Forecasting Skill Limits of Nested, Limited-Area Models: A Perfect-Model Approach

RAMÓN DE ELÍA AND RENÉ LAPRISE

Département des Sciences de la Terre et de l'Atmosphère, Université du Québec à Montréal, Montreal, Quebec, Canada

BERTRAND DENIS

Recherche en Prévision Numérique, Meteorological Service of Canada, Dorval, Quebec, Canada

(Manuscript received 16 July 2001, in final form 12 December 2001)

ABSTRACT

The fundamental hypothesis underlying the use of limited-area models (LAMs) is their ability to generate meaningful small-scale features from low-resolution information, provided as initial conditions and at their lateral boundaries by a model or by objective analyses. This hypothesis has never been seriously challenged in spite of some reservations expressed by the scientific community. In order to study this hypothesis, a perfect-model approach is followed. A high-resolution large-domain LAM driven by global analyses is used to generate a ''reference run.'' These fields are filtered afterward to remove small scales in order to mimic a low-resolution run. The same high-resolution LAM, but in a small-domain grid, is nested within these filtered fields and run for several days. Comparison of both runs over the same region allows for the estimation of the ability of the LAM to regenerate the removed small scales.

Results show that the small-domain LAM recreates the right amount of small-scale variability but is incapable of reproducing it with the precision required by a root-mean-square (rms) measure of error. Some success is attained, however, during the first hours of integration. This suggests that LAMs are not very efficient in accurately downscaling information, even in a perfect-model context. On the other hand, when the initial conditions used in the small-domain LAM include the small-scale features that are still absent in the lateral boundary conditions, results improve dramatically. This suggests that lack of high-resolution information in the boundary conditions has a small impact on the performance.

Results of this study also show that predictability timescales of different wavelengths exhibit a behavior similar to those of a global autonomous model.

1. Introduction

Limited-area models (LAMs) are powerful tools for predicting and studying weather patterns and have been used by the scientific community for some time (see references provided by White et al. 1999). Over the last decade there has been an explosion in the use of these models in a variety of research and operational applications because of their ability to perform, in local high-resolution studies, without the enormous computational cost of a global model at the same resolution. In some cases the objective is to run simulations or forecasts at a higher resolution than that given in the initial and boundary conditions, with the expectation that the increase in model resolution, which sometimes implies an improvement in both the dynamics and physics, enhances the quality of the simulation. A fundamental hypothesis underlying the use of LAMs is, hence, their ability to generate meaningful small-scale features that are absent in the initial and boundary conditions. In short, this implies that small-scale features are generated by the model independently of the small-scale features present in reality but absent in the initial and lateral boundary conditions. This independence may be attributed to the ability of the larger scales to regenerate the smaller scales (as if they remain in a ''latent'' state), or may mean that surface forcings (e.g., mountains, lakes, etc.) play an important role in their excitation.

In spite of the importance of the aforementioned hypothesis, a surprisingly small number of studies have been devoted to proving it. However, a number of studies carried out within the last 15 years have produced results that are relevant for this topic, especially those related to predictability in LAMs. Anthes et al. (1985) proposed two opposite points of view: a pessimistic one, which argues using turbulence theory that predictability in smaller scales is more limited than it is in larger scales due to the shorter overturning time; and an optimistic one, which suggests that relevant mesoscale meteorological phenomena are highly organized (far from tur-

Corresponding author address: Ramón de Elía, Département des Sciences de la Terre et de l'Atmosphère, Université du Québec à Montréal, B.P. 8888, Succ. Centre-ville, Montréal, QC H3C 3P8, Canada.
E-mail: relia@sca.uqam.ca

© 2002 American Meteorological Society

Unauthenticated | Downloaded 12/09/23 10:03 PM UTC

bulent) and therefore exhibit long-term predictability. Several researchers performed experiments that were interpreted as favorable to the optimistic approach. Anthes et al. (1985) reported that predictability in nested LAMs is different from that of global forecast models. Using ensemble integrations of a LAM nested with objective analyses at the lateral boundaries, they showed that errors in the initial conditions do not grow beyond an asymptotic value that is much smaller than the value expected for the case of total loss of correlation (as would the case with a global model). This result suggested the possibility that LAMs possess some kind of ''extended predictability.'' Errico and Baumhefner (1987) expanded this work to study individual scales by means of spectral analyses, and confirmed the results for each spatial scale.

Shortly after, this particular characteristic of LAMs was widely acknowledged. Vukicevic and Paegle (1989) mention in their introduction that, ''All the studies of predictability which uses local models show decay or no growth of the domain integrated root mean squared error throughout the forecast.'' Further research in this area by Anthes et al. (1989), Warner et al. (1989), Vukicevic and Errico (1990), Berri and Peagle (1990), Zeng and Pielke (1993), Giorgi et al. (1993), Jones et al. (1995), Giorgi and Marinucci (1996), and Peagle et al. (1997) confirmed previous results and described the sensitivity of the results to different parameters such as domain size, topography, etc. The influence of errors in the boundary conditions was also studied and was found to be much more important than sensitivity to initial conditions. In addition, Peagle et al. (1997) found that, without the existence of the driving boundaries, errors in small scales tend to grow, confirming that extended predictability is not a property of the scales under study—usually meso-α—but is a consequence of nesting. However, Boer (1994) did find an increase in predictability of small scales in a global model, attributable mostly to the stationarity of mountain-induced disturbances.

Notwithstanding the evidence gathered by years of research, part of the scientific community remains unconvinced of the capability of nested LAMs to reproduce small scales faithfully. In a report of the Working Group on Numerical Experiment (WGNE 1999), it is argued that questions concerning this point remain to be answered. A review of the articles already mentioned in this introduction lends support to this point of view, since authors found some results that did not allow for a simple interpretation. In one of the experiments of Anthes et al. (1985), errors in some variables grow linearly for 72 h. Since several sources of error were present in this experiment, subsequent experiments concentrate on simpler, better-defined problems that showed no error growth. However, the first result is not explained in light of the others. In Vukicevic and Paegle (1989) part of the article is devoted to a theoretical study in which it is shown, using a simple barotropic model, that short Rossby–Haurwitz (R–H) waves have less predictability than long ones. They concluded that, ''The difference between R–H wavenumber 2 and R–H wavenumber 4 results suggests that the boundary constraint may not be enough to suppress the error growth if the flow contains smaller scale waves.'' Van Tuyl and Errico (1989) found, using a mesoscale model, that the self-interaction of large scales does not contribute significantly to small scales, which suggests that the recreation of small scales may not be controlled by the large scales. In Berri and Peagle (1990), experiments with a small-domain high-resolution model display sensitivity to initial conditions, while experiments with the same model at 10 times lower resolution and larger domain do not.

It is interesting to note that in most articles concerning this topic, the problem of the effect of one-way nesting is not thoroughly analyzed. In few articles (e.g., Anthes et al. 1985) there is a comparison between the output fields of the nested model and the driving fields. In general, several runs of the LAM are performed for the same boundary conditions but for slightly different initial conditions, and the outputs of these runs are then used for predictability studies. Unfortunately, this widespread procedure leaves the study of the nesting per se out of the question. For this reason, the information provided by such experiments does not shed much light on the question of the LAMs ability to recreate small-scale information; it only describes the internal variability of the model.

The WGNE (1999) in its annual report suggested to construct an experiment to study the downscaling in LAMs. Following this suggestion, Laprise et al. (2000) presented results of such an experiment using a LAM-generated dataset to drive the same LAM but in a smaller domain. In order to replicate the effect of low-resolution nesting data, fields provided by the driving model to be used as lateral boundary and initial conditions were smoothed. The authors found ''no evidence for extended predictability of scales that are not forced through the lateral boundary conditions,'' challenging most of the results presented to date. On the other hand Denis et al. (2001), following a similar approach, studied the ability of a regional climate model to reproduce the high-resolution variability that had been removed form its lateral boundary conditions, and found that the model reproduced rather well the original small-scale information; in this case, the model was not asked to simulate the data in a deterministic day-by-day basis but to simulate its climate statistics. The present study continues the methodology followed by the last two previously mentioned articles, but concentrates on the short-term evolution of weather systems, as in Laprise et al. (2000).

As discussed by Giorgi and Bi (2000) when studying sensitivity experiments with LAMs, the presence of internal variability should be taken into consideration. For this reason, a predictability study precedes the analysis of the downscaling abilities of the model. Each one is discussed using a different set of experiments with a

Unauthenticated | Downloaded 12/09/23 10:03 PM UTC

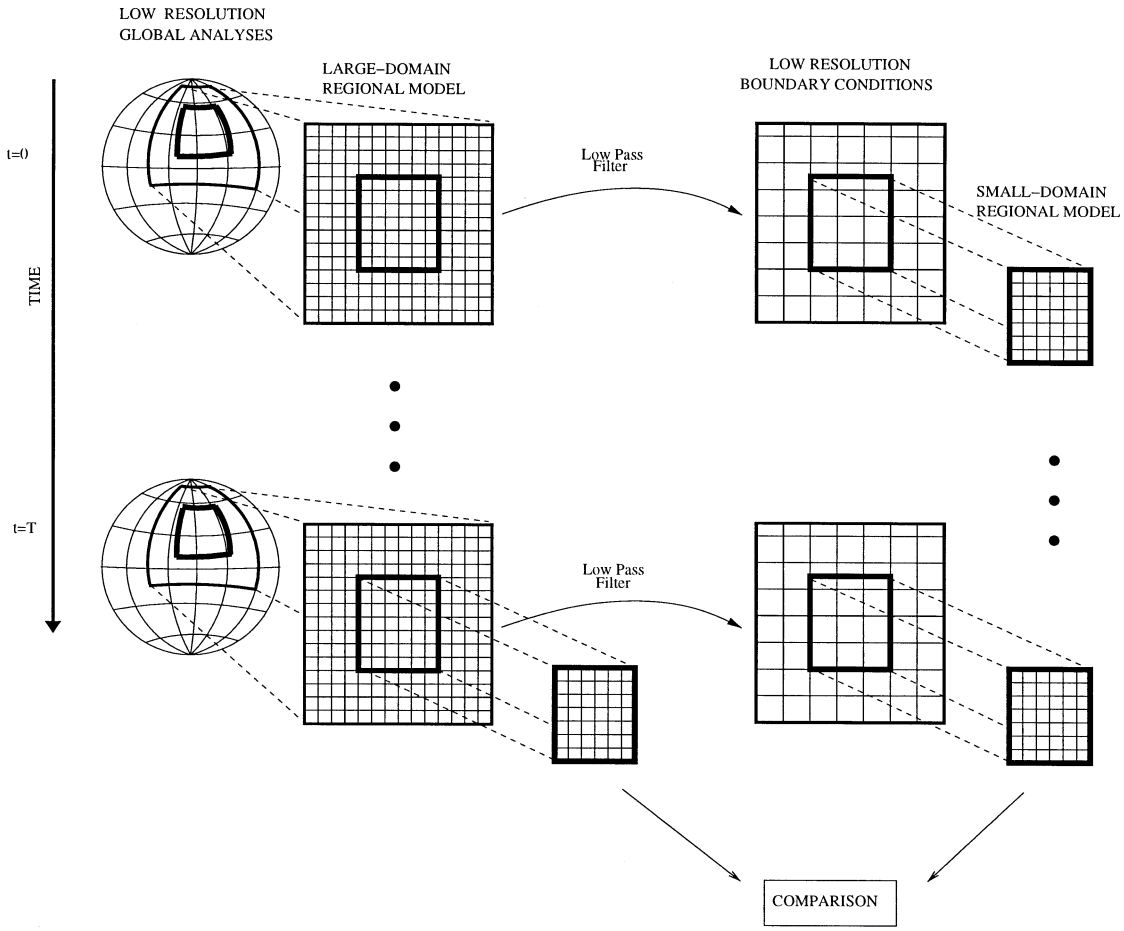

FIG. 1. Schematic of the experimental design. (left) Low-resolution global analyses are used to drive the LAM in the large domain. Fields obtained by this simulation are then used to drive the LAM in a small domain (located within the large domain), after being filtered to mimic low resolution conditions. (right) After a time T of integration, fields from both runs can be compared for the overlapping region to evaluate small-scale regeneration.

perfect-model approach, in which a LAM is nested with data generated by the same model, but in a larger domain. Section 2 describes the experimental design and the characteristics of the LAM, while section 3 presents the description and results of predictability and downscaling experiments. A summary and conclusions are given in section 4.

2. The experimental framework

The original proposal in the WGNE (1999) report suggested the approach of the ''identical twin'' paradigm, with ''a very high resolution global model as a control and a simulation with a LAM identical to that of the global model.'' Such an experiment would permit a comparison between the two models inside the regional grid and, hence, an assessment of the ability of the regional model to replicate the global model. Many other experiments can also be performed with this setup. For example, by smoothing the global fields, a realistic representation of the data sparseness may be achieved. By driving the LAM with this filtered data, it would then be possible to evaluate the ability of the arrangement to re-create the small-scale features present in the global model prior to filtering.

There are many factors that make such an experiment impractical, however, especially the computational cost. Furthermore, it may be considered unnecessary since the only area of interest in the global grid is the surroundings of the regional grid. A more pragmatic approach could be to run a single regional model on two different domain sizes: a large one that plays the role of the global model, and a small one located inside the previous one. The large-size domain LAM can be nested with objective analyses for a given period of time, and after a spinup time it will develop its own variability. The second domain, small enough to be far from the boundaries, can be driven by the large one, using exactly the same model and the same grid spacing. Figure 1 is a schematic of the experimental design. On the left, the time evolution of the large-domain LAM driven by low-resolution global analyses is represented. On the right,

Unauthenticated | Downloaded 12/09/23 10:03 PM UTC

TABLE 1. Parameters in model simulations.

Parameter	Value
Time step	15 min
Grid-point spacing	45 km (true at 60°N)
Large domain	196 × 196 grid points × 18 levels
Small domain	100 × 100 grid points × 18 levels
Large domain driven by	12-h NCEP analyses
Small domain driven by	3-h large-domain simulation

the time evolution of the small-domain LAM, driven by filtered large-domain LAM-produced fields, is shown. Since both the small-domain and the large-domain run have the same grid spacing, a comparison at all resolved scales is possible.

The LAM used in the following experiments is the Canadian Regional Climate Model (CRCM) described in Caya and Laprise (1999). It consists of a limited-area gridpoint nonhydrostatic model that uses a three-time-level semi-Lagrangian semi-implicit time-marching scheme. The nesting technique is one way, and was developed by Robert and Yakimiw (1986) and tested by Yakimiw and Robert (1990), based on the work of Davies and Turner (1977). The nesting zone region is nine points wide along the lateral boundaries, in which the horizontal velocity components are relaxed toward those from the driving model. The grid uses a polar-stereographic projection true at 60° latitude, and a Gal-Chen vertical coordinate. A complete description of the dynamical formulation of the CRCM, including the nesting implementation, can be found in Bergeron et al. (1994) and Laprise et al. (1997). The physical parameterization is described in Caya and Laprise (1999), although the present version includes the moist convective scheme of Kain and Fritsch (1990). The time evolution of the sea surface temperature (SST) was imposed by linearly interpolating monthly mean climatological data. Table 1 describes some important parameters used in the simulations of both the large and small domains. The choice of updating the boundary information of the small-domain LAM every 3 h came as a compromise between the necessity of not affecting the short waves entering the domain, and the intention to resemble operational setups. With this value, in a weather system with a speed of 10 m s^{-1}, wavelengths shorter than 100 km are affected, while the grid spacing allows for wavelengths longer than 90 km. Figure 2 shows the layout and location of the domains. The ratio between domain sizes follows the recommendations of Giorgi and Mearns (1999), who suggest that in order to study an area of interest of length scale L, the boundaries should be removed by a distance $L/2$. Considering the small domain as the area of interest with length scale L, the large domain should then have a length scale $2L$.

A 35-day integration of the CRCM is performed over the large domain, nested with National Centers for Environmental Prediction (NCEP) objective analyses starting 27 January 1993. This high-resolution simulation

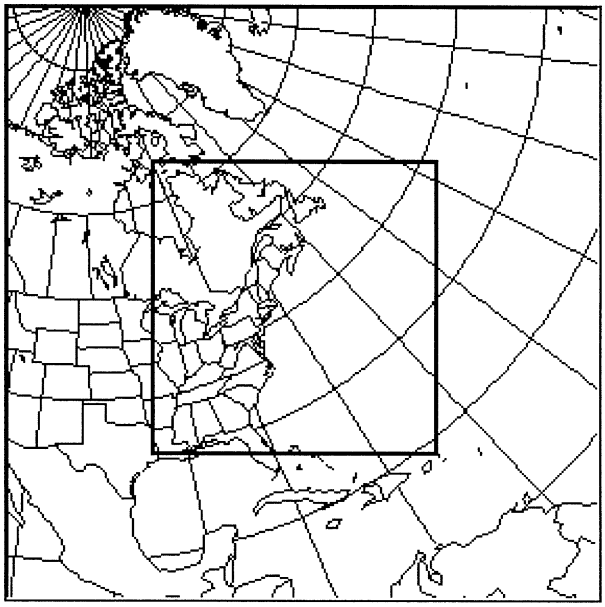

FIG. 2. Large and small integration domains.

(''reference run'' hereafter) becomes the ''truth'' with which other runs will be compared. Several experiments with the small domain are performed in which some variation is introduced either in the boundary conditions or in the initial conditions. For all cases, 24 4-day integrations of the LAM are performed in the small domain starting on 1 February and then at successive 24-h intervals. Figure 3 describes the integration schedule. In order to achieve statistical stability, results are estimated using the 24 runs of the small-domain CRCM. In this way, for example, an n-h integration ensemble average implies the average over 24 different n-h integrations, beginning 1 day apart.

3. Results

In order to gain further physical insights a scale analysis was performed on the obtained fields, and this constitutes an important part of this study. Difficulties in producing meaningful spectra from nonglobal grids have forced researchers to seek reliable algorithms (e.g., Errico 1985). In this work, results obtained using the discrete cosine transform (DCT) are presented (Denis et al. 2001, 2002). Computations were also performed using the algorithm of Errico (1985), and these provided comparable results.

The subregion of the nested LAM computational domain over which the spectral analysis must be performed is also a delicate matter. If the entire computational domain is used, the influence of lateral boundary nesting information will contaminate the results. If the area chosen to carry the spectral analysis is very far from the boundaries, the amount of data is reduced considerably, resulting in poor spectra. Experiments showed

Unauthenticated | Downloaded 12/09/23 10:03 PM UTC

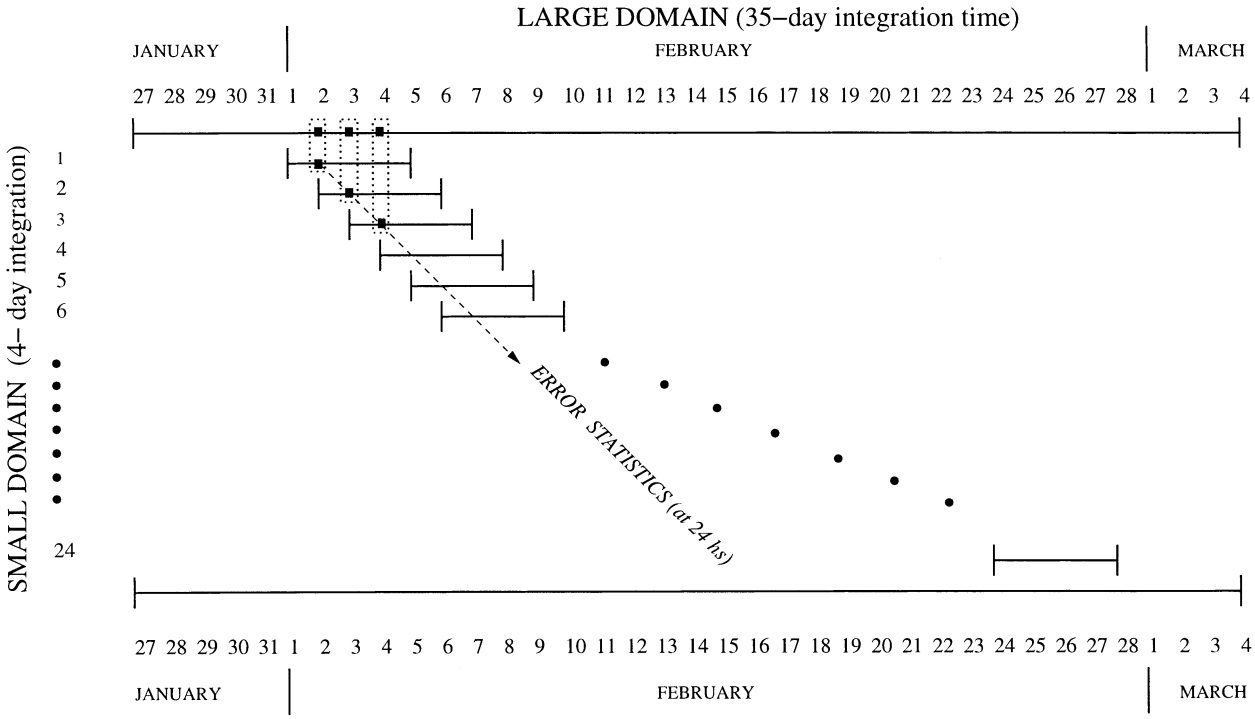

FIG. 3. Schematic of the models' integration schedule. The reference run is represented by the upper and lower long horizontal lines. Short horizontal lines depict the beginning and ending of small-domain LAM runs. The dashed line indicates the cases considered for a study of average error after 24 h of integration. Small squares inside dotted boxes signal the individual comparisons.

that by avoiding the nesting zone, variability inside the subregion was almost uniform. Hence, results are based on the analysis of a subregion of 80 × 80 within the 100 × 100 small domain.

Results presented below will concentrate on the analysis of the vorticity fields at 850 hPa. Other levels and other variables were carefully inspected, and results did not vary substantially. Nevertheless, certain advantages in the selected field and level influenced our decision: (i) the vorticity spectra has considerable energy in the small scales, which permits clear visibility of small perturbations and minimizes the error of the spectra estimation, as shown by Denis et al. (2002); (ii) the 850-hPa level is high enough not to be disrupted by topography, but low enough to display substantial energy in the small scales. For purposes of illustration, other variables are also shown in some cases. It is worth mentioning that by choosing a pressure level far from the surface, the topographic effects are less noticeable. This implies that results should be interpreted cautiously, not allowing a straightforward generalization to the surface fields.

a. Predictability

Predictability was studied by performing model integrations over the small domain without filtering the driving data (from the large domain), but introducing a small perturbation into the initial conditions. This was done by interpolating the driving data from model Gal-Chen levels into pressure levels, and then back to model levels. This procedures mimics, to some extent, the GCM–LAM mode of operation. As expected, inertio–gravity waves are generated in the first few time steps but disappear promptly. As Errico and Baumhefner (1987) explained, ''the fastest gravity waves do not strongly interact with the more slowly varying, and more important synoptic systems. Therefore, they only weakly affect the solution differences of such systems.''

Figure 4a shows a time sequence of the square root of the average spectrum, for the difference between the 850-hPa vorticity fields of the reference run and the perturbed simulations, normalized by the average vorticity spectrum of the reference run. This normalized spectrum may be interpreted as the normalized root-mean-square (rms) difference between the fields as a function of wavenumber. It can be seen that the growth is highly dependent on wavenumber, being very limited for small wavenumbers and almost reaching the critical value associated with uncorrelated signals ($\sqrt{2}$) for large wavenumbers. This behavior, found in all studied variables (wind, temperature, geopotential, specific humidity, precipitation, and divergence), suggests the existence of three different regimes: (i) synoptic-scale features that remain highly correlated after many hours of integration owing to forcing exerted by the lateral boundary conditions, (ii) mesoscale features that behave randomly after less than 2 days because of inherent

Unauthenticated | Downloaded 12/09/23 10:03 PM UTC

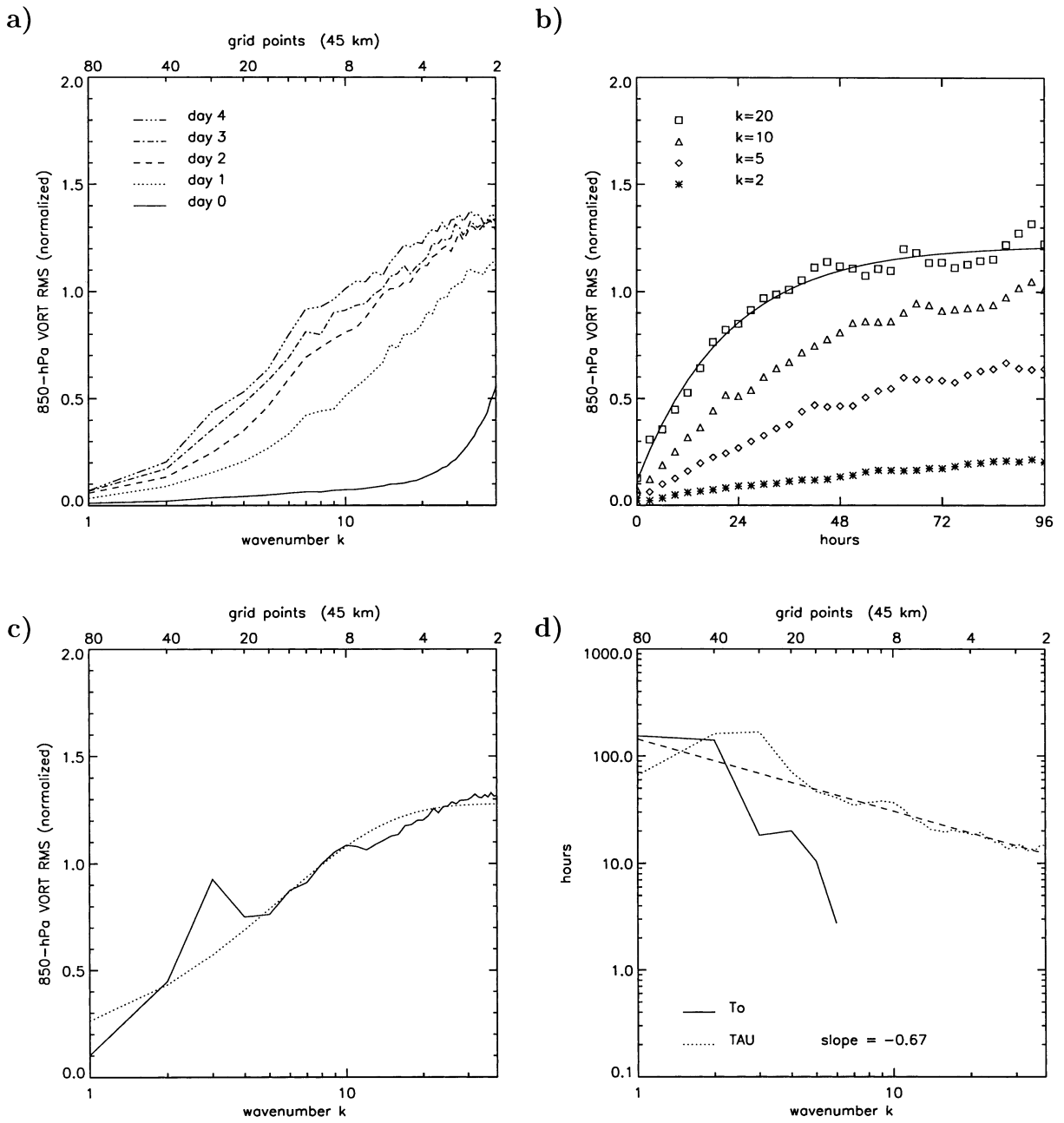

FIG. 4. Normalized RMS difference for the 850-hPa vorticity fields, between the reference run and the perturbed small-domain run. (a) The rms as a function of wavenumber for days 0–4; (b) the time evolution of four chosen wavelengths, as well as an example of the curve defined in (1) fitting wavenumber $k = 20$; (c) the asymptotic values obtained by fitting each wavenumber with (1); and (d) the values of the parameters t_0 and τ obtained by fitting the time evolution of the different wavenumbers with (1), the dashed line indicating a linear fit, for wavenumbers larger than $k = 4$, with the slope value printed at the lower bottom right.

predictability limits, and (iii) an intermediate band whose properties seem to resist a simple interpretation.

The temporal evolution of selected wavenumbers is displayed in Fig. 4b. It shows that, although all wavenumbers tend to reach different asymptotic values, each scale possesses a particular timescale in which these values are reached. The time evolution of the normalized rms has been fit with a curve defined as

$$\text{RMS} = B - Ae^{-t/\tau}, \tag{1}$$

where the parameter τ is related with the timescale of the error growth and B is the asymptotic value to which the RMS converges after long integration times. The parameter A can be better understood if expressed as $A = B \exp(-t_0/\tau)$, where t_0 represents the time before $t = 0$ when the RMS for a given wavelength was identically zero. Then (1) can be rewritten as

Unauthenticated | Downloaded 12/09/23 10:03 PM UTC

$$\text{RMS} = B[1 - e^{-(t - t_0)/\tau}]. \quad (2)$$

The degree of freedom represented by t_0 could have been removed, but exploration of results suggested keeping it. Since the size of errors at the initial time are scale dependent, there are regions of the spectrum in which RMS is already large at $t = 0$ (see solid line in Fig. 4a). The parameter t_0 can be interpreted as the amount of time it should have taken a very small but finite perturbation at a given wavenumber to reach the actual size of the perturbation present at time zero. Since this number is a function of the size of the initial perturbation, we considerer it as physically unimportant.

Figure 4c shows the asymptotic value B obtained for each wavenumber. The curve, as expected, resembles those observed in Fig. 4a after 4 days of integration. Figure 4d displays the obtained values of the timescale τ as a function of wavenumber in a log–log diagram. The straight line fitted to wavenumbers larger than $k = 4$ suggests that τ can be expressed as

$$\tau = ck^d, \quad (3)$$

with a slope $d = -0.67$. This power law was not specific to the vorticity at 850 hPa but was present in all the studied variables and at all levels. As an additional example of this, the parameter τ for temperature, geopotential, specific humidity (all of them at 850 hPa), and 3-h precipitation are shown in Fig. 5. It can be seen that for temperature (Fig. 5a) and geopotential (Fig. 5b) results are noisy for small wavelengths. This is due to the fact that variables that contain very little energy in the shortest wavelengths are sensitive to error in the spectral estimation, as discussed in Denis et al. (2002). Specific humidity (Fig. 5c) and precipitation (Fig. 5d), with less steep spectra, display results very similar to that of vorticity (Fig. 4d).

Lorenz (1969) found that each scale of motion has an intrinsic finite period of predictability; for a global model it was shown that this limit varies inversely with wavenumber, which implies a relation $\tau \sim k^d$, with slope $d = -1$. Since our experiment provided only one time series, the error in the estimation of d is unknown. However, estimations using different periods of the time series, as well as different variables, gave values differing by about 0.4. Because of the inaccuracy of this estimation it would be unrealistic to claim that this LAM exhibits a different behavior from the global model. However, results for all variables seem to suggest a slope of $d > -1$, which may indicate a slower loss of predictability. These results imply that sensitivity to initial conditions is present at all wavelengths.

This sensitivity, however, does not evolve toward a total loss of correlation. Because of the information provided at the lateral boundaries, differences asymptote to values smaller than or equal to $\sqrt{2}$, with smaller values at large scales. A complete parameterization of the evolution of the normalized RMS according to wavelength can be obtained by using (1), where the parameter B can be approximated by fitting the curve obtained in Fig. 4c with the function used in (1), while τ can be expressed as in (3). In this way, the normalized RMS can be approximated by

$$\text{RMS}\ (k, t) = C(1 - e^{-k/\kappa})(1 - e^{-t/ck^d}), \quad (4)$$

where C and κ are obtained by fitting the curves as described above. Results show that the asymptotic value for long periods of times and large wavenumbers, the parameter C, is always close to $\sqrt{2}$, as expected, but some small variations were found. Figure 6 depicts the parameterized normalized RMS for vorticity as a function of wavenumber k and time t, which may be compared to the experimental data displayed in Fig. 4a. Although this curve has been obtained for vorticity at 850 hPa, all variables analyzed (wind, temperature, geopotential, specific humidity, precipitation, and divergence) display similar characteristics. This parametric representation seems to summarize well the average properties of the normalized RMS as a function of wavenumber and time. In fields with very steep spectra (e.g., geopotential), the ''deterministic'' region predominates, resulting in low values for the total rms error. In noisier fields such as vorticity, the ''turbulent'' region has more importance, resulting in larger values for the total rms.

The shape of the curve presented in Fig. 6 shows that one-way nesting mostly controls the error growth at large scales, despite the presence of all wavenumbers in the boundary conditions. This curve can be interpreted as the highest level of accuracy that this model can achieve under this configuration and, therefore, is a landmark to be compared to in other experiments.

Results show that for the shorter scales the loss of correlation is almost total. This seems to contradict the experience of many forecasters who claim that the existence of surface forcing enhances the predictability of small scales, and which was confirmed more than a decade ago by Vukicevic and Errico (1990). In fact, two reasons might help to make this effect unnoticeable here: (i) as is mentioned in the beginning of this section, the chosen level may not contain much information regarding the surface forcing, and (ii) one distinctive feature of the spectral analysis is that it gives integrated values over the entire domain, diluting the localized effects of the surface forcings (e.g., Appalachians, land–ocean contrast) with the surrounding homogeneity.

b. Downscaling ability

When small-scale information is absent in the boundary and initial conditions, the challenge to the LAM is to regenerate small scales that are similar to the original data. In order to perform these experiments, the reference run was filtered and later used as the initial and boundary conditions for the small-domain LAM. The smoothing of data was performed with the same DCT spectral filtering mentioned in the beginning of section 3 (see Fig. 8, where the responses for different cut fre-

Unauthenticated | Downloaded 12/09/23 10:03 PM UTC

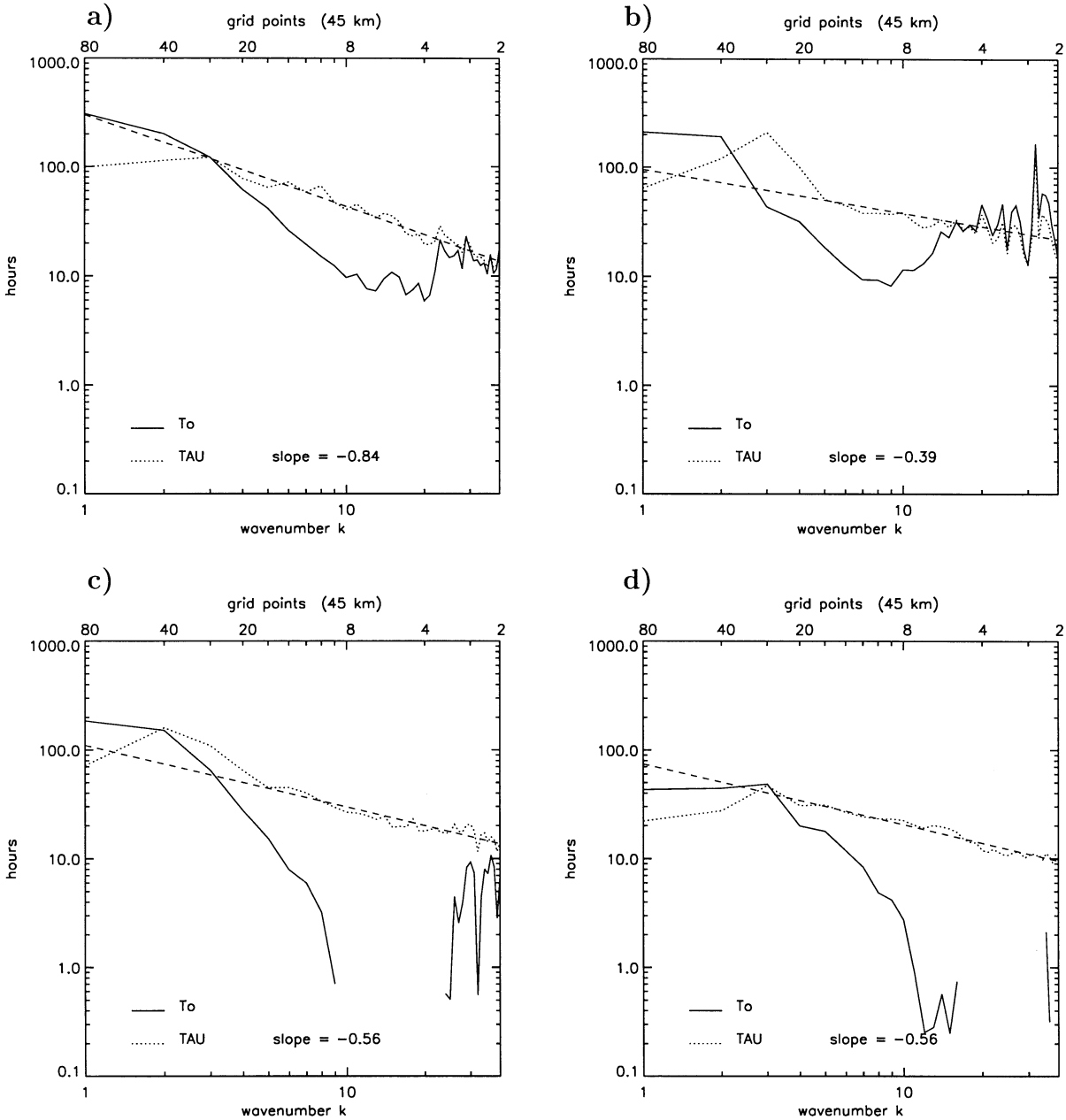

FIG. 5. Values of the parameters t_0 and τ obtained by fitting the time evolution of wavenumbers larger than $k = 4$, as in Fig. 4d but for (a) temperature at 850 hPa, (b) geopotential at 850 hPa, (c) specific humidity at 850 hPa, and (d) 3-h precipitation.

quencies of the low-pass filter are displayed as solid lines). This particular shape of the filter was chosen because of its similarity to the way in which data from low-resolution global models project into LAMs: Since not all wavenumbers present in the sphere exist in the regional grid, the abrupt truncation of wavenumbers in the global grid is reflected in a smoother way in the regional domain.

Several experiments with different cut frequencies were performed. Table 2 lists the different cases, indicating the minimum resolved wavelength in kilometers and grid points, the equivalent jump J between resolutions of the driving data and the LAM, and the equivalent resolution for a global model. Figure 7 shows an example of data in the small domain before and after filtering for J8.

Before studying the rms differences between the filtered small-domain runs and the reference runs, an evaluation of the variability created by the small-domain LAM is needed. For this purpose, it is useful to analyze the evolution of the spectrum of the small-domain run normalized by the reference run spectrum (average of

Unauthenticated | Downloaded 12/09/23 10:03 PM UTC

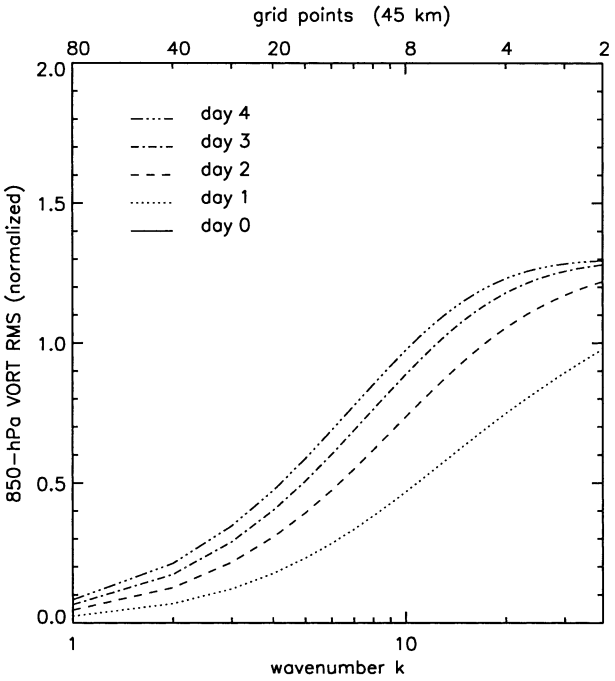

FIG. 6. Normalized RMS difference for the 850-hPa vorticity fields, between the reference run and the perturbed small-domain run, as in Fig. 4a, but for the analytical expression (4). Initial time "day 0" lies over the zero line.

TABLE 2. Resolutions obtained by filtering the reference run with different cut frequencies.

Resolved λ (km)	Grid points	Jump	Spherical harmonics
360	8	J4	T120
720	16	J8	T60
1440	32	J16	T30
2880	64	J32	T15

all cases). Figure 8 displays the time evolution of the square root of the normalized average spectrum, for the vorticity field at 850 hPa for J4, J8, J16, and J32. This can be thought of as the normalized standard deviation for each wavenumber k. A total of 96 h, every 3 h, are displayed in each case, starting at $t = 0$. The starting time illustrates the shape of the filters, having no variability at the removed, large wavenumbers, and the variability of the reference run at small wavenumbers (where the normalized standard deviation is 1).

In all cases, the small-domain LAM eventually generates variability at every scale. As more scales are filtered, however, the more time it takes to regenerate variability. For J4, illustrated in Fig. 8a, for example, it takes approximately 15 h to reach a value close to that of the reference run, while for J32 shown in Fig. 8d it takes more than 36 h. In addition, the asymptotic values reached in time decrease somewhat with increasing filtering. This is illustrated by a subtle but clear minimum at wavenumber $k = 10$ in Fig. 8c (J16), which implies that for this wavenumber variability remains somewhat smaller than that in the reference run. This problem is

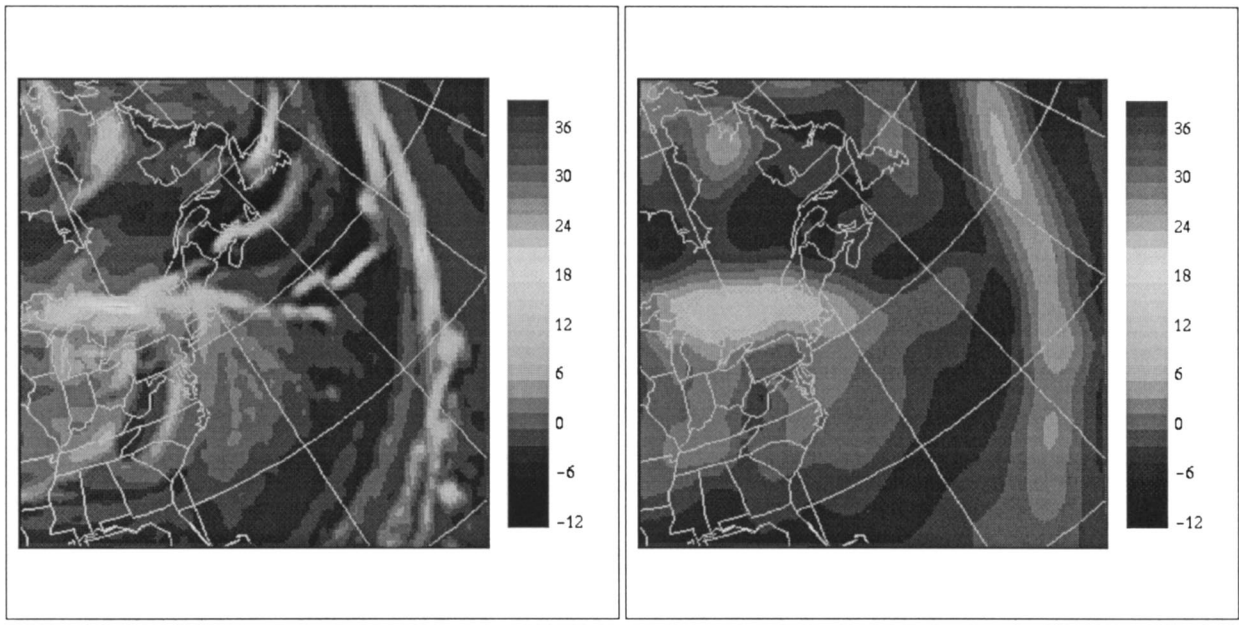

FIG. 7. Vorticity field at 850 hPa (a) prior to filtering and (b) after filtering. The resolution jump is J8, and the units are in 10^{-5} s^{-1}.

Unauthenticated | Downloaded 12/09/23 10:03 PM UTC

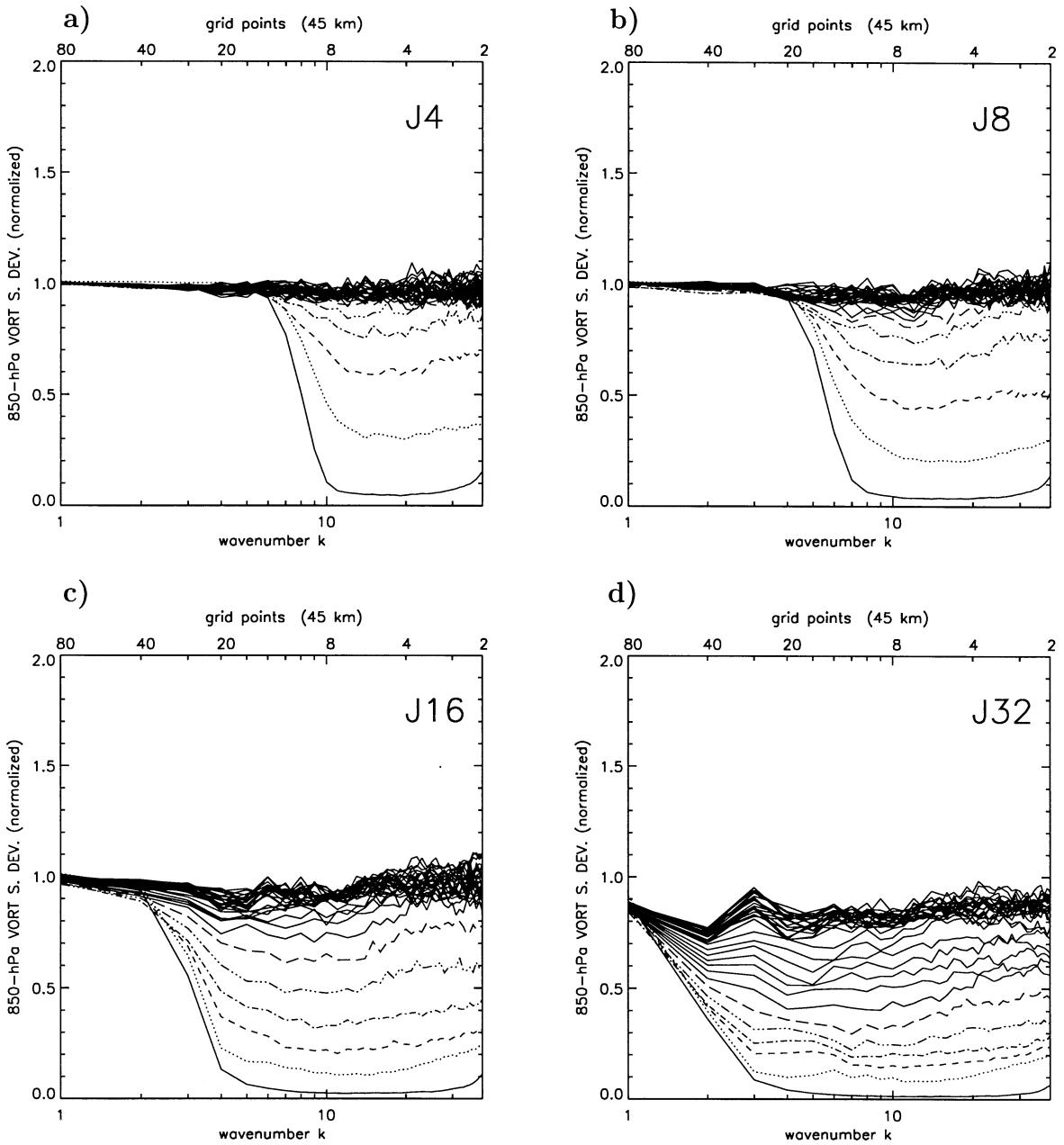

FIG. 8. Normalized standard deviation of the 850-hPa vorticity field for all wavenumbers. Values are plotted every 3 h for (a) J4, (b) J8, (c) J16, and (d) J32. The initial time (first solid line starting from the bottom) illustrates the corresponding filter response.

even more evident in Fig. 8d (J32), where wavenumbers $k = 1$ and $k = 2$ were strongly affected by filtering.

It is interesting to note that, for a given filtering value, the variance in all wavenumbers that are absent in the initial and lateral boundary conditions seems to grow in time at the same rate. This is evinced by the fact that, for larger wavenumbers, the curves representing different times are almost parallel horizontal straight lines. An estimation of the timescale of the downscaling process can be obtained by fitting the time evolution of the standard deviation of the wavelengths affected by truncation with (1) as was done for Fig. 4b. These fittings showed that the timescale τ is weakly dependent on wavelength, and was found to be for all the studied variables: J4, $\tau \sim 6$ h; J8, $\tau \sim 8$ h; J16, $\tau \sim 12$ h; and J32, $\tau \sim 18$ h. The values for J4 and J8 are smaller than those of the predictability timescales depicted in Fig. 4d, which shows variations between 10 and 40 h for different wavelengths. This is a necessary result if the aim is to recreate the small scales before the internal variability takes over.

The results presented above show that the one-way

Unauthenticated | Downloaded 12/09/23 10:03 PM UTC

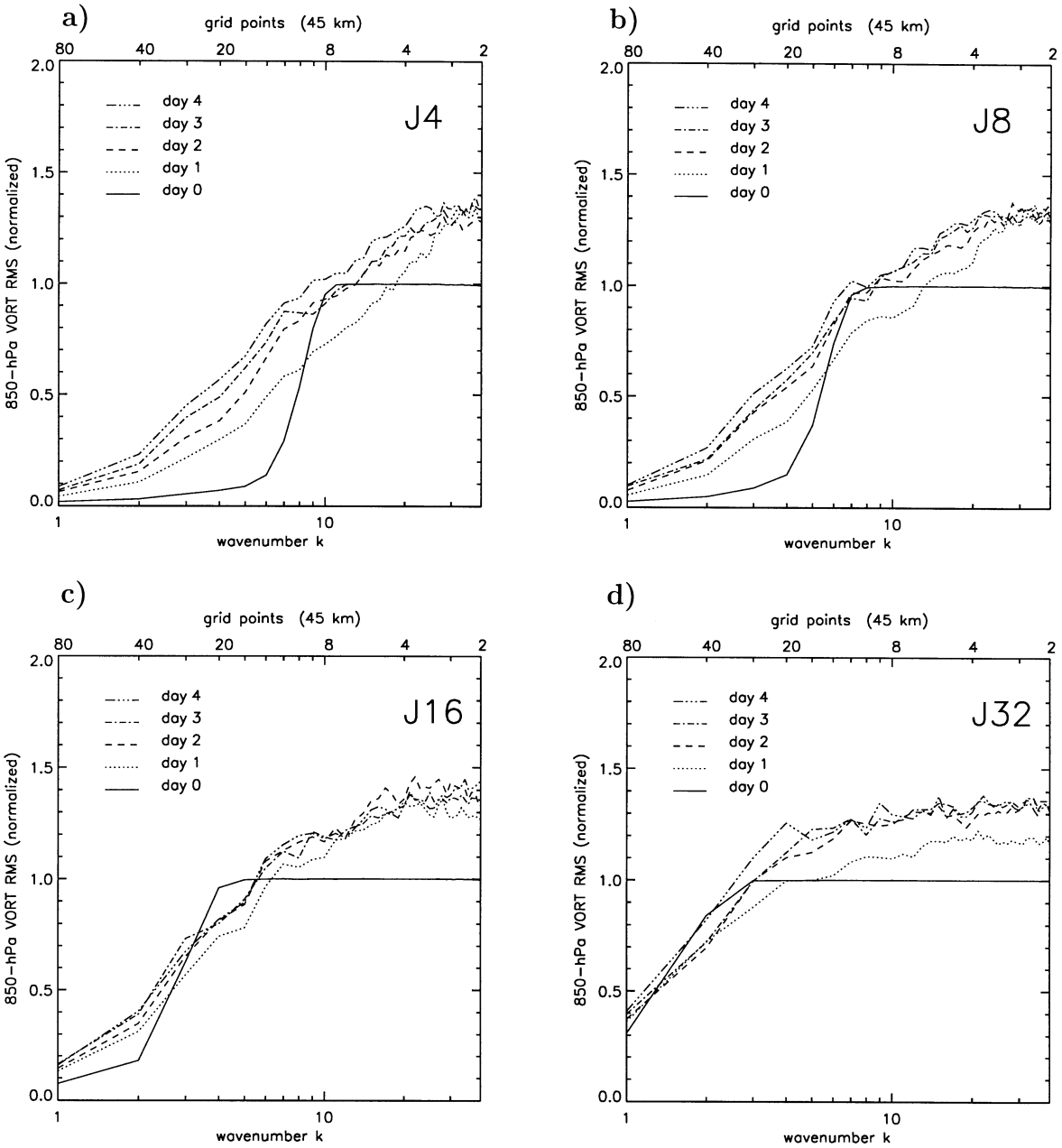

FIG. 9. Normalized RMS difference for the 850-hPa vorticity fields as a function of wavenumber for days 0–4, as in Fig. 4a, but for (a) J4, (b) J8, (c) J16, and (d) J32.

nesting develops finescale features when nested with sufficiently high resolution in the initial and in the lateral boundary conditions. The almost exact reproduction of the variance of the reference run (ratio close to 1) can be explained by the fact that both the reference run and the filtered run use the same LAM and similar but differently truncated boundary conditions.

The evaluation of the forecasting skill requires more than studying the ability to reproduce the right level of variability: the quality of the small scales generated also needs to be studied. To study the accuracy of the re-created small-scale features, we now examine the normalized RMS difference between the filtered small-domain run and the reference run. Figure 9 shows the normalized RMS difference as is defined for Fig. 4a but for different resolution jumps in initial and lateral boundary conditions. The normalized RMS = 1 for the removed length scales at the initial time illustrates well the effect of filtering.

For nearly all scales error increases with time, although there is a narrow band of scales near the limit of filtering where the error decreases in time for a short

Unauthenticated | Downloaded 12/09/23 10:03 PM UTC

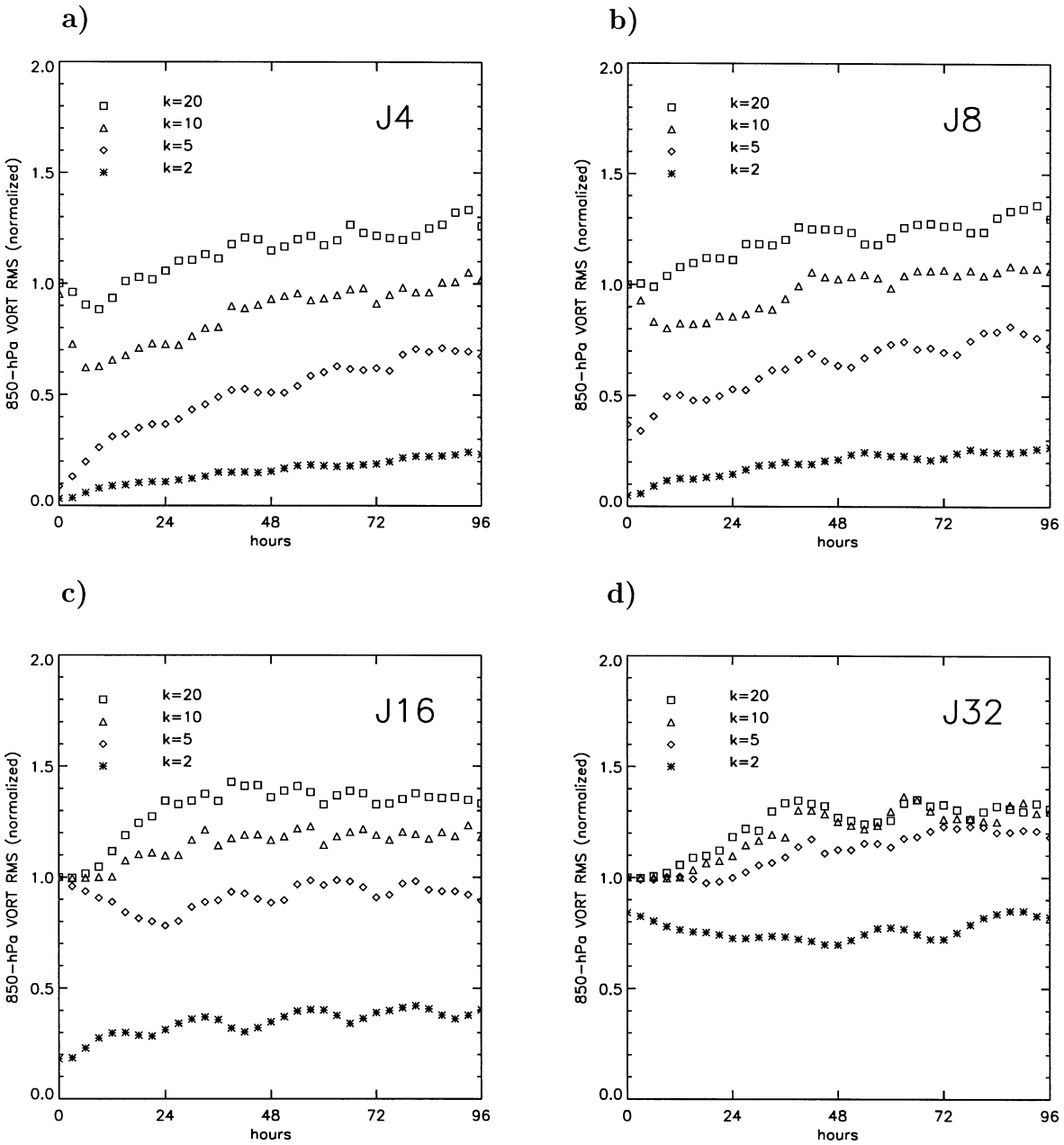

FIG. 10. Time evolution of the normalized RMS difference for the 850-hPa vorticity fields for four chosen wavenumbers, as in Fig. 4b, but for (a) J4, (b) J8, (c) J16, and (d) J32.

period. After around 2 days of integration, values become nearly asymptotic, and by days 3 and 4 they seem already quite stable. In comparison with Fig. 4a, the four cases reach asymptotic values at a higher RMS, although cases J4 and J8 (panels a and b) appear to be quite similar. Figure 10 displays the temporal evolution of four selected wavenumbers for each of the resolution jumps shown in Fig. 9. In general it can be seen that some wavenumbers affected by filtering (e.g., $k = 10$, in Figs. 10a and 10b) tend to diminish the normalized RMS during the first hours of integration, and soon after this a loss of precision takes over. The amount of time it takes this minimum to be reached varies with case and wavenumber, ranging from 6 h for $k = 10$ in J4 (Fig. 10a) to 24 h for $k = 5$ in J16 (Fig. 10c).

Comparisons between Figs. 10 and 4b shed some light regarding the behavior of the downscaling. As was noted in the previous section, the time evolutions displayed in Fig. 4b represent the landmark against which the quality of the downscaling should be compared. The optimal situation would have been a rapid reduction in the RMS of those wavelengths affected by filtering, until

Unauthenticated | Downloaded 12/09/23 10:03 PM UTC

loss of predictability brings up the RMS in a way similar to that in the slightly perturbed case of Fig. 4b. Results show that the reduction of RMS in all cases shown in Fig. 10 is not as fast and marked as might have been expected. For example, the lowest RMS value for $k = 10$ in the case J4 (reached at 6 h, as shown in Fig. 10a) is 0.6, while at the same time and the same wavelength for the slightly perturbed experiment RMS = 0.2 (Fig. 4b). For shorter wavelengths the situation is even worse, as can be seen with $k = 20$ in J8 case (Fig. 10b). Here, there is only a hint of a reduction of RMS at 6 h, and afterward this values increase monotonically (with the exception of a few minor oscillations that might be associated with a daily wave).

Although it is difficult to evaluate the importance of the RMS reduction in the first hours of integration, there is no doubt that some wavelengths do not show any relevant sign of reduction. These results suggest that the downscailing is, from a deterministic point of view, not as efficient as had been hoped.

c. Interpreting the error

In order to evaluate the importance of the errors displayed in Figs. 4a and 9 we propose two different but related ways of interpreting the results. The first method consists of a theoretical evaluation of the impact on the rms of a solid shift of a field, while the second studies the effect of a temporal displacement with exact data.

1) SOLID SHIFT

Let us first consider a two-dimensional field $f(x, y)$ that can be written as a Fourier series as

$$f(x, y) = \mathrm{Re}\left[\sum_{k,l=0}^{N} A_{kl} e^{i2\pi(kx+ly)}\right], \tag{5}$$

where A_{kl} is the amplitude; k and l are wavenumbers in the x and y directions, respectively; and i the imaginary unit. A solid shift in the field can be represented as $f(x - \Delta x, y - \Delta y)$, where Δx and Δy are the displacement in the x and y directions, respectively. Then the difference $f(x, y) - f(x - \Delta x, y - \Delta y)$ can be written as

$$f(x, y) - f(x - \Delta x, y - \Delta y) = \mathrm{Re}\left\{\sum_{k,l=0}^{N} A_{kl}[1 - e^{i2\pi(k\Delta x+l\Delta y)}]e^{i2\pi(kx+ly)}\right\}. \tag{6}$$

After rearranging the terms it can be shown that the spectral variance S_{kl} of this difference can be expressed as

$$S_{kl} = |A_{kl}|^2 |1 - e^{i2\pi(k\Delta x+l\Delta y)}|^2. \tag{7}$$

Defining S_M as the average spectrum with $M^2 = k^2 + l^2$ we then obtain

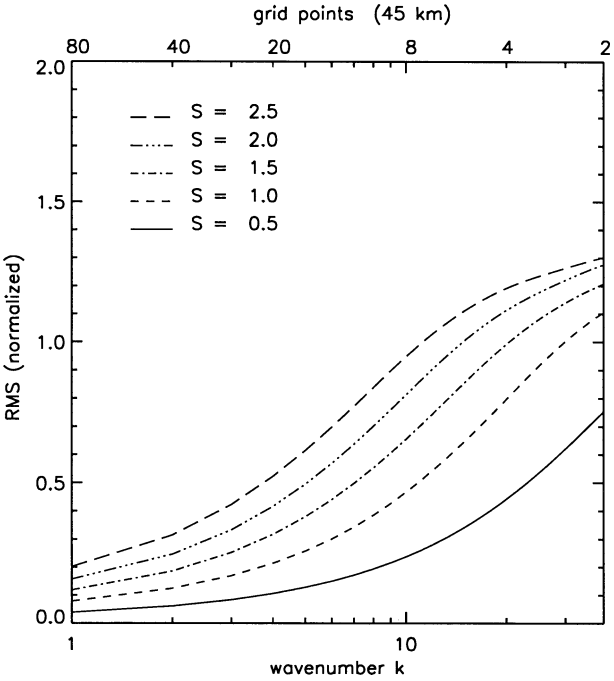

FIG. 11. Normalized RMS as a function of wavenumber for an average solid shift in a hypothetical field. Plotted lines illustrate values for different distributions of shifts, having standard deviations S = [0.5, 1.0, 1.5, 2.0, 2.5, 3.0] in gridpoint units.

$$S_M = \frac{1}{M}\sum_{k=1}^{M} S_{k\sqrt{M^2-k^2}} = \frac{2}{M}\sum_{k=1}^{M} A^2_{k\sqrt{M^2-k^2}}[1 - \cos 2\pi(k\Delta x + l\Delta y)]. \tag{8}$$

Since the normalized $\mathrm{RMS}^2_M = S_M/A^2$, by assuming for simplicity that the amplitudes A_{kl} are identical, that the displacement is in only one direction, and using the identity

$$\sum_{k=1}^{M} \cos k\alpha = \frac{\sin 2\pi(M + 1/2)\Delta x}{2 \sin 2\pi M\Delta x/2} - \frac{1}{2}, \tag{9}$$

we obtain

$$\mathrm{RMS}^2_M = 2\left\{1 - \frac{1}{2M}\left[\frac{\sin 2\pi(M + 1/2)\Delta x}{\sin 2\pi M\Delta x/2} - 1\right]\right\}. \tag{10}$$

We can estimate an average value of RMS^2_M for several cases assuming, for example, that the shift Δx follows a normal distribution $N_{0,S}$ with nil average value (no systematic shift) and a variance S^2. Then,

$$\overline{\mathrm{RMS}^2_M} = \int_{-\infty}^{\infty} \mathrm{RMS}^2_M(x) N_{0,S}(x)\, dx. \tag{11}$$

Figure 11 displays a numerical solution of the previous integral for S = [0.5, 1.0, 1.5, 2.0, 2.5] in gridpoint units. The curves represent the average normalized RMS for solid displacements Δx of the field, having a normal

Unauthenticated | Downloaded 12/09/23 10:03 PM UTC

distribution with zero mean displacement and standard deviation S. Since the mean displacement is nil, both positive and negative directions are allowed.

This diagram may be thought of as the effect of phase error of weather systems on the RMS for each wavelength. As expected, an error in the position of the weather system affects more strongly the shorter wavelengths. It can be seen that for $S = 0.5$ (i.e., a standard deviation of half grid point in the distribution of spatial shifts), the rms error obtained is similar to that of 1 day of integration in the LAM for $k = 1$ and $k = 2$ (see Fig. 4a). For larger wavenumbers, it is clear that a 1-day integration produces errors closer to $S = 1.0$. For longer integration periods, it can be seen that for small wavenumbers, rms errors are comparable to those produced by $S < 1$, while for intermediate wavenumbers (e.g., $k = 10$), rms errors correspond to larger values of S.

Larger error for the intermediate wavenumbers may come from error in the relative position of short waves with respect to the weather system, or in their intensity. It is important to note that since error asymptotes near normalized RMS $= \sqrt{2}$, a comparison of large RMS values gives little information regarding overall field differences.

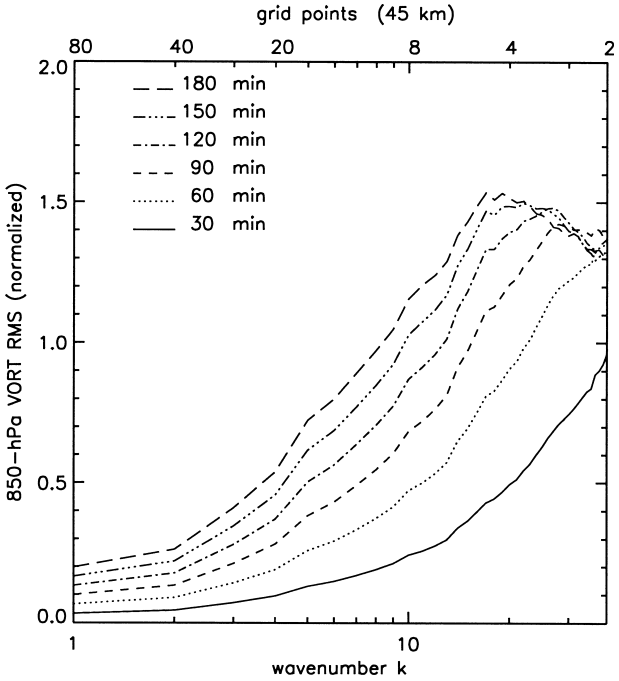

FIG. 12. Normalized RMS as a function of wavenumber for an average temporal shift. Plotted lines illustrate values for different shifts Δt = [30, 60, 90, 120, 150, 180] min.

2) TEMPORAL DISPLACEMENT

In order to complement the previous study of solid spatial displacement, a temporal shift is also performed. The rms difference between successive fields of the same time series can also be interpreted as the rms error of a delayed perfect forecast. The normalized RMS difference between successive fields Δt apart for the vorticity field at 850 hPa is therefore computed. Averages of 4 days' worth of data, 30 min apart, are displayed in Fig. 12 for different values of Δt = [30, 60, 90, 120, 150, 180] min.

It is interesting to notice that a 60-min delay of a perfect forecast (Fig. 12) seems to have a similar effect on all wavenumbers as an integration of a LAM during 1 day (Fig. 4a). It can be seen that a 90-min delay of a perfect forecast generates an error in the long waves similar to that of many days of integration in the predictability study of Fig. 4a. A longer time delay is required to generate an error in intermediate wavenumbers (e.g., wavenumber $k = 7$), comparable to that of a few days of integration: to reach a comparable rms error to that found in the predictability study, the perfect forecast should be delayed by around 180 min. Large wavenumbers reach saturation error in both cases, making comparison unprofitable.

Results from both the solid and temporal shift suggest that an important part of the error in small scales might be explained as a small error in the phase of the weather systems, and visual inspection confirmed that this was the case in several instances. This happens in spite of the fact that the long waves are imposed at the boundaries, and that both simulations use the same LAM. It is also clear from these computations that the rms is a very sensitive error measurement tool and that results should be interpreted under this perspective.

One issue that surfaces in this analysis is that the requirement that short wavelengths be ''in phase'' imposes restrictions beyond what is necessary for a very acceptable weather forecast (e.g., a delay of less than 30 min). What is implicit in this discussion is that by going into smaller scales the forecaster not only desires a good spatial resolution of weather phenomena but also a higher accuracy in the timing. This may not necessarily be the case since even if the future allows for a grid spacing of 40 m, the forecaster will not be concerned with delays of the order of the 2 s. Continual improvement in spatial resolution does not change the fact that human activities remain mostly the same.

d. Experiments with high-resolution initial conditions and low-resolution boundary conditions

In some cases, a region of dense data is surrounded by an area of relatively sparse data (e.g., continental United States). When a LAM is utilized over this kind of region, the initial conditions include small-scale features while the lateral boundary conditions that drive the model have coarser resolution.

This particular distribution of data was represented by running a set of experiments identical to the ones presented in Table 2, with the exception that in this case

Unauthenticated | Downloaded 12/09/23 10:03 PM UTC

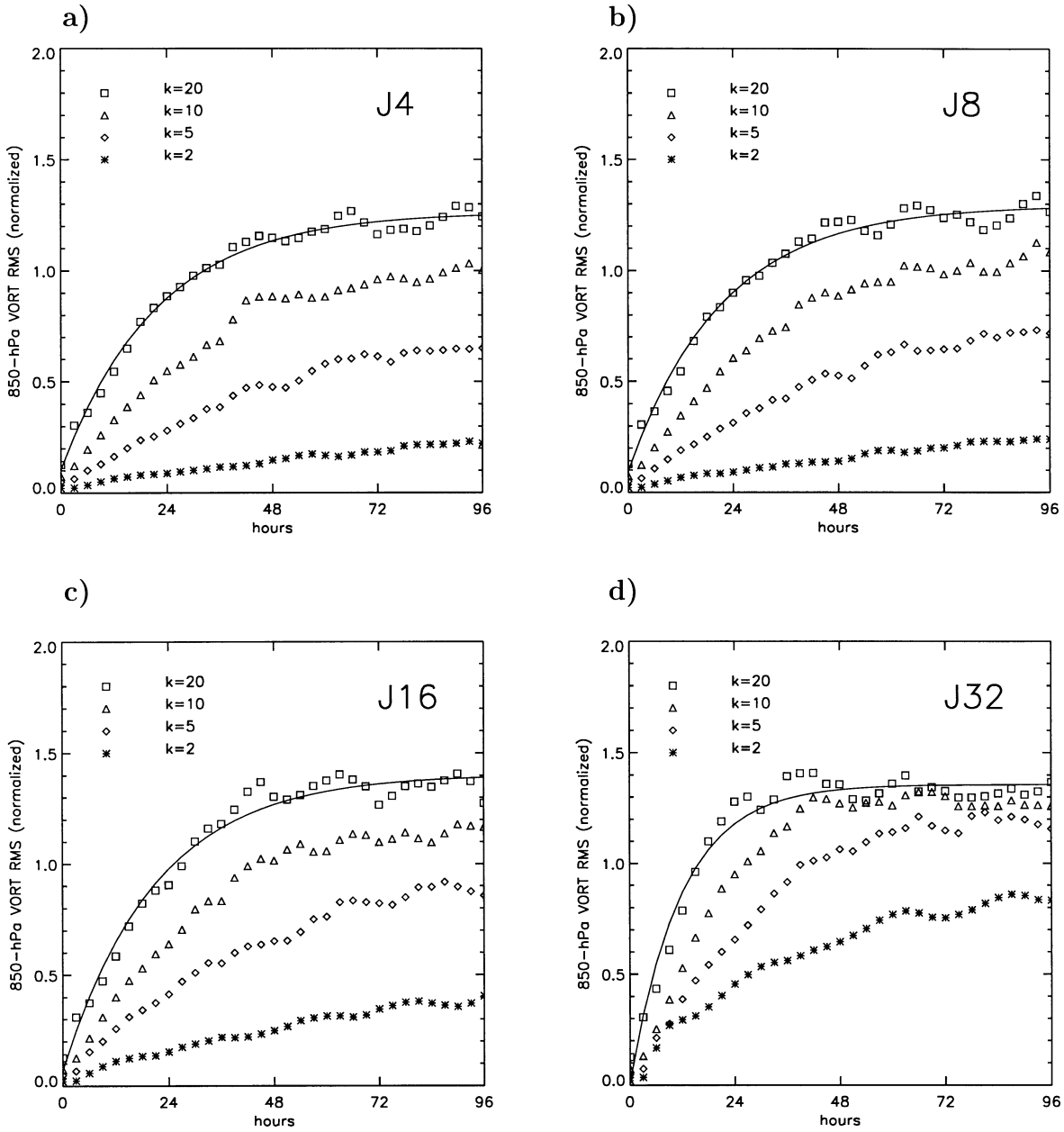

FIG. 13. As in Figs. 4b and 10 but for the case where only lateral boundary conditions are filtered (initial conditions remain unfiltered).

the initial conditions were not filtered, thus maintaining the quality of the reference run at initial time. Figure 13 shows the time evolution for selected wavenumbers for the same resolution jumps in lateral boundary conditions as were shown in Fig. 10. Comparisons between the respective panels indicate that cases with similar resolution in the boundaries (e.g., Fig. 10a and Fig. 13a) reach the same asymptotic values, suggesting, as shown by previous studies, that the rms difference becomes independent of the initial conditions after a certain period. On the other hand, for the first 24 h the RMS growth for J4 and J8 (Figs. 13a and 13b, respectively) does not differ much from the case with high-resolution information in both initial and boundary conditions (Fig. 4b). These experiments show the very important impact of the initial conditions on the rms difference in the first hours of integration. This is quite striking for the cases with smaller resolution jumps (J4 and J8), in which a similar growth rate of the rms difference with respect to the high-resolution driven model is found. This seems to suggest that if boundaries are set, as is usually recommended, far from the region of interest, the quality of the simulation is rather insensitive to the resolution of the driving data. This can be interpreted in two ways,

Unauthenticated | Downloaded 12/09/23 10:03 PM UTC

as good news highlighting the remarkable job of a LAM given the right initial conditions, and as a warning that increasing resolution in the lateral boundary driving data may only have a very limited impact on the rms error.

In this experiment the model was not required to downscale information but to generate a reliable simulation from filtered lateral boundary conditions. The success may be due to either the ability to maintain the evolution of small-scale features, despite the degraded lateral boundary conditions, or that the rate of degradation due to the internal variability is faster than the corruption introduced by the lateral boundary conditions. In either case the results seem to support the rationale of limited-area modeling provided that good quality high-resolution initial and good quality low-resolution lateral boundary conditions are provided.

4. Concluding remarks

The ability of LAMs to recreate small-scale features that were absent in the initial and/or the lateral boundary conditions was studied. For this purpose, a regional model (CRCM) was used to perform several runs of the same resolution in two different domains: one large, nested with NCEP analyses, and one a small, located within the large one and nested with the values obtained by this large-domain simulation. This experimental setup allowed us to perform different studies in a perfect-model environment, thus concentrating on the nesting effect rather than on intrinsic model errors. Hence our results can be interpreted as the upper limit of skill achievable with an imperfect LAM nested with imperfect initial and lateral boundary conditions. Results presented here are essentially based in the analysis of vorticity at 850 hPa, but results in other variables showed similar characteristics.

Our predictability studies suggest that the initial growth rates in nested LAMs may not differ substantially from those of global models. In global models, however, the asymptotic limit of the normalized RMS difference reaches $\sqrt{2}$, while for LAMs, the asymptotic value reached by the normalized RMS is less than or equal to $\sqrt{2}$, varying with length scale. For small scales the asymptotic values is close to $\sqrt{2}$, while for large scales the asymptotic value is much smaller than $\sqrt{2}$, illustrating the concept of ''extended predictability'' first introduced by Anthes et al. (1985). Results show that one-way nesting mostly controls the error growth at large scales, even when all wavenumbers are present in the boundary conditions. No signal was found to suggest that surface forcings extend the predictability, although it is discussed that the chosen height level, the selected region, and the characteristics of the spectral analysis do not highlight it.

When the initial and lateral boundary conditions of the LAM are degraded by smoothing or filtering, the LAM is able to regenerate the variability lost by filtering. The recreated small scales, however, differ from the original ones as revealed by the rms study. Differences with the reference run grow with time in most wavenumbers, with the exception of a narrow band close to the truncation wavenumber whose *RMS* decreases during the first hours. This decrease in RMS is not very pronounced, and after some time, all wavenumbers reach asymptotic RMS values that are higher than initial values. The importance of the decrease in RMS seems difficult to assess, and may require a different approach to the data analysis. However, it is clear that from a deterministic point of view the downscaling is not very efficient.

When the initial conditions contain high-resolution information and the boundary conditions are filtered, the normalized RMS difference evolves similarly to the one produced by the unfiltered case. This suggests that the quality of the simulation is rather insensitive to the resolution of the driving data, which implies on one hand that the rationale behind the LAMs is sound, and on the other the inefficiency of increasing the resolution in the lateral boundary conditions as a means of improving the simulation quality.

An important point is suggested by the study in section 3c, which compares the effect of both a solid displacement of the weather system and a delayed perfect forecast on the rms. These comparisons suggest that phase delays of the order of some hours may produce the same error as that produced by a lack of predictability after a few days of integration. This comparison raises the question of the fairness of demanding precision in time proportional to wavelength, which is an implicit assumption in our scale analysis.

It may be of interest to repeat these experiments by nesting the model through the nudging of large scales (von Storch et al. 2000; Biner et al. 2000) and thereby eliminating completely the error in the large scales. With this approach, error in the smaller scales could not come from phase errors induced by slight errors at larger scales.

Throughout the text it has been mentioned that the use of an rms error measure imposes restrictions on the generalizability of the conclusions. Of no less importance is the difficulty of this or any other score skill to summarize the predominant features of a given experiment. This is why the visual inspection of meteorological fields has been carried out carefully. In the predictability and in the J4 and J8 downscaling experiments, fields with sharp spectra (e.g., geopotential) look almost identical, with some differences in phase or intensity when the field includes an intense weather system. Variables that allowed for small-scale inspection because of their spectral characteristics (e.g., vorticity) show that small scales associated with weather systems are normally recreated but sometimes at the wrong place and with a different shape.

High-resolution LAMs have been used for many different applications. If the application aims to increase the accuracy of the prediction in intensity and phase at

Unauthenticated | Downloaded 12/09/23 10:03 PM UTC

a given point, results presented here suggest there is a limited gain by running a high-resolution model because of the short predictability limit of small scales and the inefficiency of the downscaling phenomena. Some additional research, however, is needed to estimate the significance of the gain in the first hours of integration, which may be of importance according to the subjective experience of many forecasters. As White et al. (1999) put it: ''numerical products available from recently emerging mesoscale model guidance provide valuable insight, but still lack the specificity to justify point-wise warnings''.

The results of Denis et al. (2001), which employed a similar methodology to the one presented here but for climate timescales, do lend confidence as to the ability of high-resolution LAMs to gain accuracy in a statistical sense.

Caution must be exerted in generalizing these tentative conclusions because too little is known about their sensitivity to factors not considered here, such as domain size, grid spacing, nesting frequency, dynamics, physics, nesting method, season, geographical location, topography, score skill, etc. These results, however, constitute a warning against overenthusiastic expectations regarding mesoscale predictions with LAMs.

Acknowledgments. We are very grateful to the scientific and technical staff of the Canadian Regional Climate Model Group (CRCM) at UQAM for their unlimited accessibility, and to Claude Desrochers for maintaining an efficient computing environment for the CRCM group. This work has been financially supported by Canadian NSERC, funding from the U.S. Department of Energy Climate Change Prediction Program (CCPP), and the UQAM regional climate modeling group. We gratefully acknowledge the Meteorological Service of Canada for granting an education leave to the third author during this study and for providing access to its computer facilities.

REFERENCES

Anthes, R. A., Y. H. Kuo, D. P. Baumhefner, R. M. Errico, and T. W. Bettge, 1985: Predictability of mesoscale motions. *Advances in Geophysics*, Vol. 288, Academic Press, 159–202.

——, ——, S. Low-Nam, and T. W. Bettge, 1989: Estimation of skill and uncertainty in regional numerical models. *Quart. J. Roy. Meteor. Soc.*, **115,** 763–806.

Bergeron, G., R. Laprise, and D. Caya, 1994: Formulation of the Mesoscale Compressible Community (MC2) model. Cooperative Centre for Research in Mesometeorology Internal Rep., 165 pp. [Available from Dr. D. Caya, Groupe des Sciences de l'Atmosphère, Département des Sciences de la Terre et de l'Atmosphère, Université du Québec à Montréal, B.P. 8888, Succ. Centre-ville., Montréal, QC H3C 3P8, Canada.]

Berri, G. J., and J. Paegle, 1990: Sensitivity of local predictions to initial conditions. *J. Appl. Meteor.*, **29,** 256–267.

Biner, S., D. Caya, R. Laprise, and L. Spacek, 2000: Nesting of RCMs by imposing large scales. Research Activities in Atmospheric and Oceanic Modeling, WMO Rep. 30, CAS/JSC Working Group on Numerical Experimentation (WGNE), WMO/TD-987, 7.3–7.4.

Boer, G. J., 1994: Predictability regimes in atmospheric flow. *Mon. Wea. Rev.*, **122,** 2285–2295.

Caya, D., and R. Laprise, 1999: A semi-implicit semi-Lagrangian regional climate model: The Canadian RCM. *Mon. Wea. Rev.*, **127,** 341–362.

Davies, H. C., and R. E. Turner, 1977: Updating prediction models by dynamical relaxation: An examination of the technique. *Quart. J. Roy. Meteor. Soc.*, **103,** 225–245.

Denis, B., R. Laprise, J. Côté, and D. Caya, 2001: Downscaling ability of one-way nested regional climate models: The big-brother experiment. *Climate Dyn.*, **18,** 627–646.

——, J. Côté, and R. Laprise, 2002: Spectral decomposition of two-dimensional atmospheric fields on limited-area domains using the discrete cosine transform (DCT). *Mon. Wea. Rev.*, **130,** 1812–1829.

Errico, R., 1985: Spectra computed from a limited area grid. *Mon. Wea. Rev.*, **113,** 1554–1562.

——, and D. Baumhefner, 1987: Predictability experiments using a high-resolution, limited-area model. *Mon. Wea. Rev.*, **115,** 488–504.

Giorgi, F., and M. R. Marinucci, 1996: An investigation of the sensitivity of simulated precipitation to model resolution and its implications for climate studies. *Mon. Wea. Rev.*, **124,** 148–166.

——, and L. Mearns, 1999: Introduction to special section: Regional climate modeling revisited. *J. Geophys. Res.*, **104,** 6335–6352.

——, and X. Bi, 2000: A study of internal variability of a regional climate model. *J. Geophys. Res.*, **105,** 29 503–29 521.

——, M. R. Marinucci, G. T. Bates, and G. De Canio, 1993: Development of a second generation regional climate model (REGCM2). Part II. Convective processes and assimilation of lateral boundary conditions. *Mon. Wea. Rev.*, **121,** 2814–2832.

Jones, R. G., J. M. Nurphy, and M. Noguer, 1995: Simulation of climate change over Europe using a nested regional climate model. I. Assesment of control climate, including sensitivity to location of boundary conditions. *Quart. J. Roy. Meteor. Soc.*, **121,** 1413–1449.

Kain, J. S., and J. M. Fristch, 1990: A one-dimensional entraining/detraining plume model and its application in convective parameterization. *J. Atmos. Sci.*, **47,** 2784–2802.

Laprise, R., D. Caya, G. Bergeron, and M. Giguère, 1997: The formulation of André Robert MC2 (Mesoscale Compressible Community) model. *Atmos.–Ocean*, **35** (André Robert Memorial Volume), 195–220.

——, M. R. Varma, B. Denis, D. Caya, and I. Zawadzki, 2000: Predictability of a nested limited-area model. *Mon. Wea. Rev.*, **128,** 4149–4154.

Lorenz, E. N., 1969: The predictability of a flow which possesses many scales of motion. *Tellus*, **21,** 289–307.

Paegle, J., Q. Yang, and M. Wang, 1997: Predictability in limited area and global models. *Meteor. Atmos. Phys.*, **63,** 53–69.

Robert, A., and E. Yakimiw, 1986: Identification and elimination of an inflow boundary computational solution in limited area model integrations. *Atmos.–Ocean*, **24,** 369–385.

Van Tuyl, A. H., and R. M. Errico, 1989: Scale interaction and predictability in a mesoscale model. *Mon. Wea. Rev.*, **117,** 495–517.

von Storch, H., H. Langerberg, and F. Feser, 2000: A spectral nudging technique for dynamical downscaling purposes. *Mon. Wea. Rev.*, **128,** 3664–3673.

Vukicevic, T., and J. Paegle, 1989: Influence of one-way interacting lateral boundary conditions upon predictability of flow in bounded numerical models. *Mon. Wea. Rev.*, **117,** 340–350.

——, and R. Errico, 1990: The influence of artificial and physical factors upon predictability estimates using a complex limited-area model. *Mon. Wea. Rev.*, **118,** 1460–1482.

Unauthenticated | Downloaded 12/09/23 10:03 PM UTC

Warner, T. T., L. E. Key, and A. M. Lario, 1989: Sensitivity of a mesoscale-model forecast skill to some initial-data characteristics, data density, data position, analysis procedure, and measurement error. *Mon. Wea. Rev.,* **117,** 1281–1310.

WGNE, 1999: Report of Fifteenth Session of the CAS/JSC Working Group on Numerical Experimentation. WGNE Rep. 14, Naval Research Laboratory, Monterey, CA, 29 pp.

White, B. G., J. Paegle, W. J. Steerburgh, J. D. Worel, R. T. Swanson, L. K. Cook, D. J. Onton, and J. G. Myles, 1999: Short-term forecast validation of six models. *Wea. Forecasting,* **14,** 84–108.

Yakimiw, E., and A. Robert, 1990: Validation for a nested grid-point regional forecast model. *Atmos.–Ocean,* **28,** 466–472.

Zeng, X., and R. A. Pielke, 1993: Error-growth dynamics and predictability of surface thermally induced atmospheric flow. *J. Atmos. Sci.,* **50,** 2817–2844.

Unauthenticated | Downloaded 12/09/23 10:03 PM UTC